The Astrophysical Journal, 834:6 (7pp), 2017 January 1 doi:10.3847/1538-4357/834/1/6
© 2016. The American Astronomical Society. All rights reserved.

MERGER-INDUCED SHOCKS IN THE NEARBY LIRG VV 114 THROUGH METHANOL OBSERVATIONS WITH ALMA

Toshiki Saito[1,2], Daisuke Iono[2,3], Daniel Espada[2,3], Kouichiro Nakanishi[2,3], Junko Ueda[4], Hajime Sugai[5], Shuro Takano[6], Min S. Yun[7], Masatoshi Imanishi[8], Satoshi Ohashi[1,2], Minju Lee[1,2], Yoshiaki Hagiwara[9], Kentaro Motohara[10], and Ryohei Kawabe[1,2,3]

[1] Department of Astronomy, The University of Tokyo, 7-3-1 Hongo, Bunkyo-ku, Tokyo 113-0033, Japan; toshiki.saito@nao.ac.jp
[2] National Astronomical Observatory of Japan, 2-21-1 Osawa, Mitaka, Tokyo, 181-0015, Japan
[3] The Graduate University for Advanced Studies (SOKENDAI), 2-21-1 Osawa, Mitaka, Tokyo 181-0015, Japan
[4] Harvard-Smithsonian Center for Astrophysics, 60 Garden Street, Cambridge, MA 02138, USA
[5] Kavli Institute for the Physics and Mathematics of the Universe (WPI), The University of Tokyo, 5-1-5 Kashiwanoha, Kashiwa, 277-8583, Chiba, Japan
[6] Physics Department, College of Engineering, Nihon University, 1 Nakagawara, Tokusada, Tamura, Koriyama, Fukushima, 963-8642, Japan
[7] Department of Astronomy, University of Massachusetts, Amherst, MA 01003, USA
[8] Subaru Telescope, 650 North Aohoku Place, Hilo, HI 96720, USA
[9] Natural Science Laboratory, Toyo University, 5-28-20, Hakusan, Bunkyo-ku, Tokyo 112-8606, Japan
[10] Institute of Astronomy, The University of Tokyo, 2-21-1 Osawa, Mitaka, Tokyo 181-0015, Japan
Received 2016 August 30; revised 2016 October 10; accepted 2016 November 3; published 2016 December 22

ABSTRACT

We report the detection of two CH_3OH lines ($J_K = 2_K$–1_K and 3_K–2_K) between the progenitor's disks ("Overlap") of the mid-stage merging galaxy VV 114 obtained using the Atacama Large Millimeter/submillimeter Array (ALMA) Band 3 and Band 4. The detected CH_3OH emission shows an extended filamentary structure ($\sim$3 kpc) across the progenitor's disks with relatively large velocity width (FWZI $\sim$ 150 km s^{-1}). The emission is only significant in the "overlap" and not detected in the two merging nuclei. Assuming optically thin emission and local thermodynamic equilibrium, we found the CH_3OH column density relative to H_2 (X_{CH_3OH}) peaks at the "Overlap" ($\sim 8 \times 10^{-9}$), which is almost an order of magnitude larger than that at the eastern nucleus. We suggest that kpc-scale shocks driven by galaxy–galaxy collision may play an important role to enhance the CH_3OH abundance at the "Overlap." This scenario is consistent with shock-induced large velocity dispersion components of ionized gas that have been detected in optical wavelength at the same region. Conversely, low X_{CH_3OH} at the nuclear regions might be attributed to the strong photodissociation by nuclear starbursts and/or a putative active galactic nucleus, or inefficient production of CH_3OH on dust grains due to initial high-temperature conditions (i.e., desorption of the precursor molecule, CO, into gas phase before forming CH_3OH on dust grains). These ALMA observations demonstrate that CH_3OH is a unique tool to address kpc-scale shock-induced gas dynamics and star formation in merging galaxies.

Key words: galaxies: individual (VV 114, IC 1623, Arp 236) – galaxies: interactions – radio lines: galaxies

1. INTRODUCTION

Bright thermal rotational transitions of methanol (CH_3OH) are often used as a tracer of extragalactic shocks, which are established by a large number of unbiased wide-band mm/sub-mm molecular line surveys toward galaxies over the last decade (Takano et al. 2014, and references therein). Extragalactic CH_3OH observations found that some of the galaxies have X_{CH_3OH} larger than $\sim 10^{-8}$ at the nuclei, arms, and bars with $\sim$100 pc resolution (e.g., IC 342; Meier & Turner 2005). Purely gas-phase chemistry cannot explain these observational evidences, because the formation process of CH_3OH in gas phase is not efficient to produce X_{CH_3OH} greater than $\sim(1$–$3) \times 10^{-9}$ (Lee et al. 1996). Alternatively, high CH_3OH abundance is believed to arise from a series of hydrogenations of CO on dust-grain surfaces under a low-temperature ($\sim$10 K) condition (Watanabe et al. 2003), because interstellar icy mantles are rich in CH_3OH ($\sim 10^{-6}$; e.g., Schutte et al. 1991). After the production on dust, it requires high temperature (i.e., hot-core chemistry; e.g., Garrod et al. 2008) or energetic heating (i.e., shock chemistry; e.g., Viti et al. 2011) mechanisms to heat the dust and then sublime CH_3OH into gas phase. On the other hand, CH_3OH molecules are easily destroyed by UV radiation due to starburst or active galactic nucleus (AGN) without shielding ($A_V \sim 5$; Martín et al. 2009). Thus, CH_3OH requires hot-core-like or shocked interstellar matter (ISM) without strong UV radiation field to achieve an observable abundance. When hot-core-like environment is excluded, CH_3OH lines become an excellent extragalactic shock tracer in molecular ISM.

However, most of the previous studies have so far mainly focused on nearby, bright galaxies, or their nuclear regions (Henkel et al. 1987; Meier & Turner 2005; Martín et al. 2006a, 2006b; Usero et al. 2006; García-Burillo et al. 2010; Aladro et al. 2011; Costagliola et al. 2011; Martín et al. 2011; Meier & Turner 2012; Davis et al. 2013; Meier et al. 2014; Takano et al. 2014; Watanabe et al. 2014; Aladro et al. 2015; Costagliola et al. 2015; Nakajima et al. 2015; Galametz et al. 2016; Nishimura et al. 2016). In this paper, we present multiple CH_3OH line observations toward the nearby merging galaxy VV 114, which are follow-up observations of our previous CH_3OH (2_K–1_K) detection at Overlap (Saito et al. 2015), in order to test kpc-scale shocks in molecular ISM due to a gas-rich galaxy–galaxy collision.

VV 114 is one of the local luminous infrared galaxies ($D_L = 87$ Mpc, $L_{IR} = 10^{11.69} L_\odot$; Armus et al. 2009). It is considered to be a mid-stage gas-rich major merger with the nuclear separation of $\sim$6 kpc. The system has a (molecular and ionized) gaseous and dust filamentary structure ($\sim$4 kpc) across

Table 1
Information of the Detected CH_3OH Lines and their Imaging Properties

Transition	Blended J_K	ν_{rest} (GHz)	ν_{obs} (GHz)	E_u (K)	$S\mu^2$	Beam Size (″)	Beam P.A. (°)	δv (km s^{-1})	Noise rms[a] (mJy beam^{-1})
2_K–1_K	2_{-1}–1_{-1}, E	96.73936	94.88251	12.5	1.21	1.47 × 1.12	−88.8	50	0.37
	2_0–1_0, A^{++}	96.74138	94.88449	7.0	1.62				
	2_0–1_0, E	96.74455	94.88760	20.1	1.62				
	2_1–1_1, E	96.75551	94.89835	28.0	1.24				
3_K–2_K	3_0–2_0, E	145.09371	142.30873	27.1	2.42	1.60 × 1.04	+67.8	20	0.69
	3_{-1}–2_{-1}, E	145.09737	142.31232	19.5	2.16				
	3_0–2_0, A^{++}	145.10315	142.31799	13.9	2.43				
	3_2–2_2, A^{--}	145.12441	142.33884	51.6	1.36				
	3_2–2_2, E	145.12619	142.34058	36.2	1.33				
	3_{-2}–2_{-2}, E	145.12639	142.34078	39.8	1.35				
	3_1–2_1, E	145.13186	142.34614	35.0	2.21				
	3_2–2_2, A^{++}	145.13346	142.34772	51.6	1.36				

Note.
[a] Noise rms in the data, which have a velocity resolution of δv.

the galaxy disks (Yun et al. 1994; Frayer et al. 1999; Iono et al. 2004, 2013; Wilson et al. 2008; Rich et al. 2011; Sliwa et al. 2013; Saito et al. 2015; Tateuchi et al. 2015), which is not found in optical, far-UV (FUV), and X-ray images (Scoville et al. 2000; Goldader et al. 2002; Grimes et al. 2006).

Our previous Atacama Large Millimeter/Submillimeter Array (ALMA) observations (Iono et al. 2013; Saito et al. 2015) revealed that the filament has multiple star-forming dense gas clumps at Overlap, one of which only has a CH_3OH (2_K–1_K) peak. In contrast, two massive clumps in the eastern nucleus, which harbor compact starburst ("SB") and putative hard X-ray AGN ("AGN"), are bright in CN, HCN, and HCO^+ lines. This indicates that VV 114 has kpc-scale chemical variations along the filament. However, since we were only able to observe 10 molecular lines, the chemical composition in the filament is not fully understood, and thus we followed up VV 114 with ALMA spectral scan mode.

We assumed $H_0 = 70\,\mathrm{km\,s^{-1}\,Mpc^{-1}}$, $\Omega_M = 0.3$, $\Omega_\Lambda = 0.7$ ($1'' = 420$ pc) throughout this paper.

2. OBSERVATIONS AND DATA OVERVIEW

We observed VV 114 using Band 3 and Band 4 of ALMA with the spectral scan mode (Mathys 2013) as a cycle 2 program (ID: 2013.1.01057.S). The correlator was configured to cover 84–111 GHz and 127–154 GHz using eight tunings. In this paper, we present the tunings containing the multiple CH_3OH (2_K–1_K) ($\nu_{obs} \sim 94.84$ GHz) and CH_3OH (3_K–2_K) ($\nu_{obs} \sim 142.24$ GHz) lines. We observed blended sets of thermal rotational transitions of CH_3OH. Detected transitions are listed in Table 1. Other transitions (e.g., $J_K = 0_0$–1_{-1}) are not robustly detected. Since such nondetections do not put meaningful upper limits in the analysis shown later, we ignore them in this paper. We will discuss some nondetected molecular lines in T. Saito et al. (2016, in preparation). The CH_3OH (2_K–1_K) data (Band 3) were obtained on 2014 July 3, 2014 July 4, and 2015 June 11 with the double-sideband system temperature (T_{sys}) of 39–103 K, whereas the CH_3OH (3_K–2_K) data (Band 4) was obtained on 2015 May 25 with T_{sys} of 47–124 K. 31 to 38 (36) 12 m antennae with the projected baseline length of 19–778 m (21–539 m) were assigned for the Band 3 (Band 4) observations. Each tuning has four spectral windows to cover each sideband. The spectral window has a bandwidth of 1.875 GHz with 1.938 MHz resolution, while they were binned together to create better signal-to-noise ratio data cubes. The total onsource time of the Band 3 and Band 4 observations are 47.4 minutes and 20.0 minutes, respectively. Neptune and Uranus were used for the flux calibration of both the bands. J0137-2430 and J2258-2758 were used for the bandpass calibration of both the bands. Either J0116-2052 or J0110-0741 was used for the phase calibration of Band 3, whereas J0110-0741 was used for the phase calibration of Band 4.

The data reduction, calibration, and imaging were carried out using CASA (McMullin et al. 2007). All maps were reconstructed with the natural weighting to minimize rms noise levels. We made the data cubes with a velocity resolution of 50 km s^{-1} (∼14.4 MHz) for CH_3OH (2_K–1_K) and 20 km s^{-1} (∼9.8 MHz) for CH_3OH (3_K–2_K). Before imaging, we combined the cycle 0 CH_3OH (2_K–1_K) data (ID: 2011.0.00467.S) in order to increase the sensitivity, and continuum emission was subtracted in the *uv*-plane. We note that we recalibrated the cycle 0 data using the Butler-JPL-Horizons 2012 model. Other imaging properties are listed in Table 1, and will be introduced in detail by T. Saito et al. (2016, in preparation). The systematic error of absolute flux scaling factor using a solar system object is 5% for Band 3 and Band 4 (Lundgren 2013). The flux densities of the bandpass and phase calibrators were in good agreement with measurements provided by the ALMA Calibrator Source Catalogue.[11] We ignore the difference of the missing flux effect between Band 3 and Band 4, since the maximum recoverable scale of the assigned configuration for the Band 3 and Band 4 observations (18″ and 13″, respectively) is comparable or larger than the filament of VV 114 detected in ^{13}CO (1–0) and dust continuum (Saito et al. 2015).

3. RESULTS

Images of the integrated intensity, velocity field, and velocity dispersion are shown in Figure 1. The total CH_3OH (2_K–1_K) and CH_3OH (3_K–2_K) integrated intensities are 0.91 ± 0.11 and 2.31 ± 0.18 Jy km s^{-1}, respectively. We checked possible blending with other species using the molecular line database Splatalogue[12] and also line detections reported by Watanabe et al. (2014), Aladro et al. (2015) and Costagliola et al. (2015),

[11] https://almascience.nrao.edu/sc/
[12] http://www.splatalogue.net/

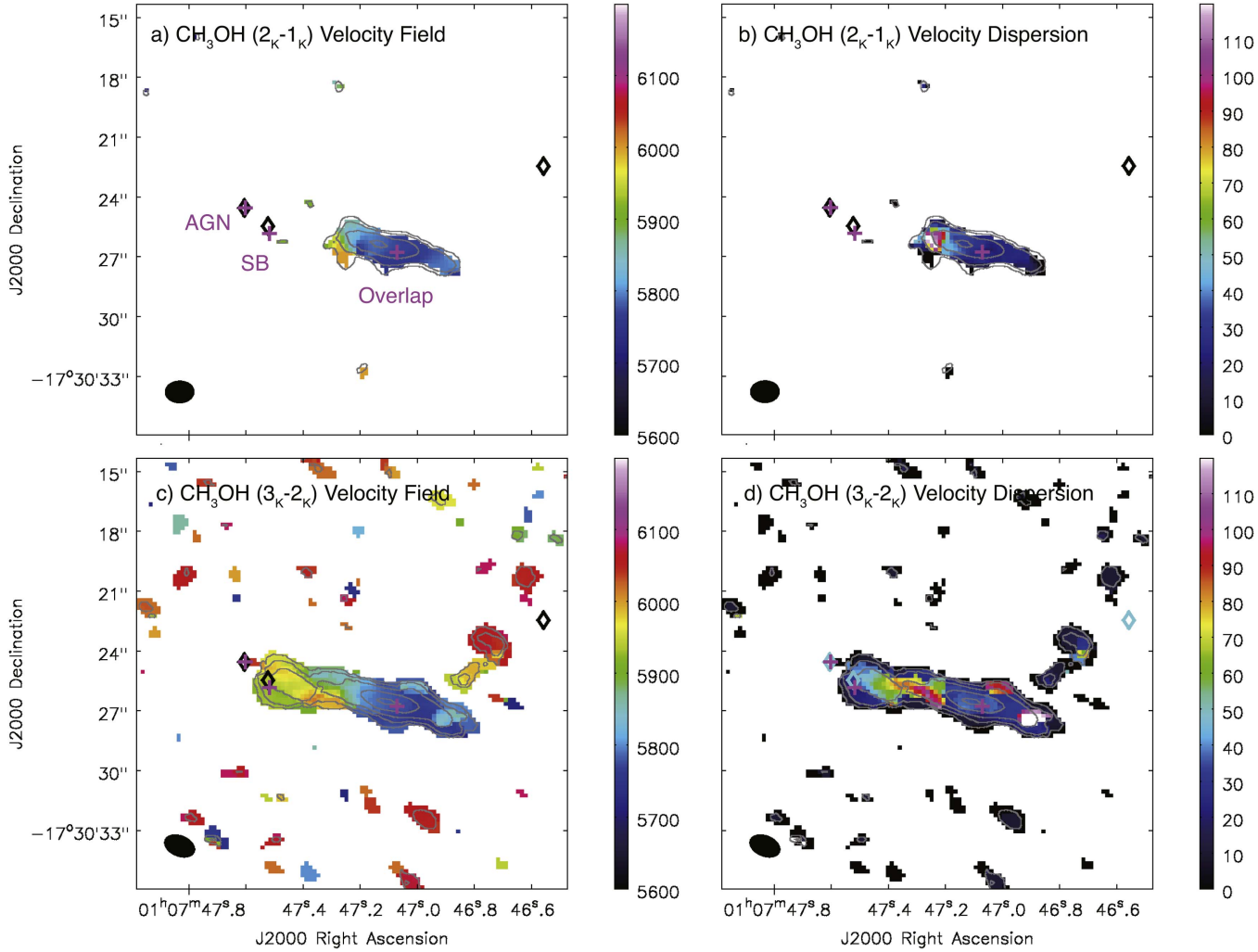

Figure 1. (a) Integrated intensity contour of CH_3OH (2_K–1_K) overlaid on the velocity field. The contours are 0.32 × (0.16, 0.32, 0.64, and 0.96) Jy beam^{-1} km s^{-1}. (b) Integrated intensity contour of CH_3OH (2_K–1_K) overlaid on the velocity dispersion. (c) The same as (a), but for CH_3OH (3_K–2_K). The contours are 0.67 × (0.08, 0.16, 0.32, 0.64, and 0.96) Jy beam^{-1} km s^{-1}. (d) The same as (c), but for CH_3OH (3_K–2_K). The crosses show the peak positions of the HCO^+ (4–3) emission. AGN, SB, and Overlap correspond to E0, E1, and W0, respectively, as defined by Iono et al. (2013). The synthesized beams are shown in the bottom-left corner. The diamonds show the K_s-band stellar nuclei.

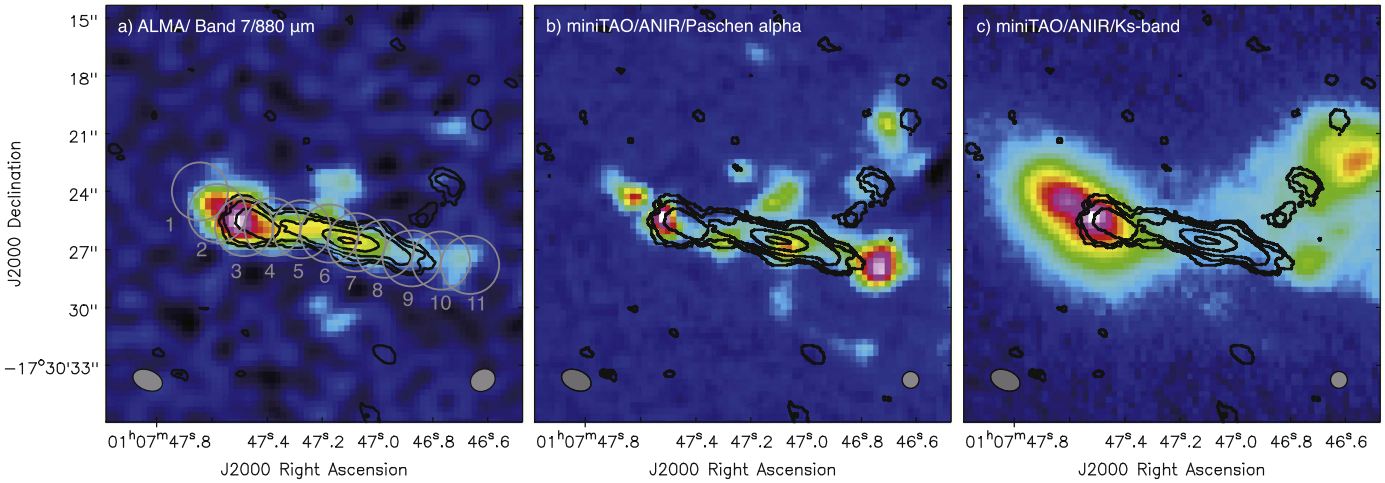

Figure 2. Integrated intensity contour of CH_3OH (3_K–2_K) overlaid on (a) 880 μm dust emission, (b) Paschen α emission, and (c) Ks-band (Saito et al. 2015; Tateuchi et al. 2015). The synthesized beam of the CH_3OH (3_K–2_K) image is shown in the bottom-left corner. The beam size of each color image is shown in the bottom-right corner. The 11 gray circles shown in Figure 2(a) are used for the photometry along the filament.

because some extragalactic line surveys reached line confusion limits. We found no potential bright lines around CH_3OH (2_K–1_K). Although there is c-C_3H_2 (3_{12}–2_{21}) (ν_{rest} = 145.08961 GHz) around CH_3OH (3_K–2_K) (ν_{rest} = 145.09–145.14 GHz), its contribution to the CH_3OH (3_K–2_K) intensities may be negligible, because any other c-C_3H_2 transitions are not robustly detected toward the Overlap region in our Band 3/4 data. This is consistent with the starburst galaxy NGC 253 that is thought to be dominated by shocks, and shows weaker c-C_3H_2 line emissions than the CH_3OH (2_K–1_K) line (Aladro et al. 2015). Toward SB (Figure 2), we detected some c-C_3H_2 transitions (e.g., $J_{KaKc} = 4_{04}$–3_{13}), which were not stronger than CH_3OH (3_K–2_K), and so CH_3OH (3_K–2_K) intensity might be slightly overestimated. However, this does not change our discussion and conclusion (see Section 4).

Figure 1 shows an extended filamentary structure, which coincides with previous molecular gas and dust images (Iono et al. 2013; Saito et al. 2015). The strongest peak is located at Overlap, whereas the emission is only marginally detected in the stellar nuclei seen in the Ks-band (Figure 2(c)). The global distribution is consistent with ^{13}CO and HCO^+ lines (molecular gas; Iono et al. 2013; Saito et al. 2015) and 880 μm continuum (dust; Figure 2(a)), although all of them except for CH_3OH show strong peaks at AGN and SB. In contrast, CH_3OH does not coincide with Paschen α emission (H_{II} regions and/or ionized gas shocks; Figure 2(b)). The Ks-band continuum, mainly tracing an old stellar component (Figure 2(c)), has no peaks at Overlap. This indicates that the CH_3OH filament of VV 114 is a relatively young structure compared with the age of the progenitor galaxies, which is likely due to a galaxy–galaxy collision as predicted by numerical simulations of a gas-rich major merger (Saitoh et al. 2009; Teyssier et al. 2010). These morphological comparisons suggest that CH_3OH lines trace a kpc-scale gas structure at the collision interface of the galaxy–galaxy interaction. To determine the physical properties of Overlap, we employ the rotation diagram method (Goldsmith & Langer 1999) in the next section.

4. LOCAL THERMODYNAMIC EQUILIBRIUM (LTE) CALCULATION OF ROTATION TEMPERATURE AND COLUMN DENSITY

Assuming LTE and optically thin conditions for the CH_3OH lines, we can estimate the column density (N_{CH_3OH}) and rotation temperature (T_{rot}) using the rotation diagram. However, we need a special treatment in the case of VV 114, because the detected CH_3OH emission was blended by multiple A-type and E-type rotational transitions (e.g., Rabli & Flower 2010) due to the coarse velocity resolution and observed large velocity widths (FWZI $\sim$ 150 km s^{-1}) as seen in a spectrum toward Region 6 (Figure 3(a)) and a position–velocity diagram along the CH_3OH filament (Figure 3(b)). By assuming that both types of CH_3OH have the same beam-averaged column density (N_{CH_3OH}), the CH_3OH flux can be expressed by using the least squares method with the following equation (e.g., Martín et al. 2006b; Watanabe et al. 2014),

$$W_\nu = \sum_i \frac{8\pi^3 S_i \mu_0^2 \nu_i N_{CH_3OH}}{3kQ_{rot}} \left\{1 - \frac{\exp(h\nu_i/kT_{rot}) - 1}{\exp(h\nu_i/kT_{bg}) - 1}\right\} \times \exp\left(-\frac{E_{u,i}}{kT_{rot}}\right), \quad (1)$$

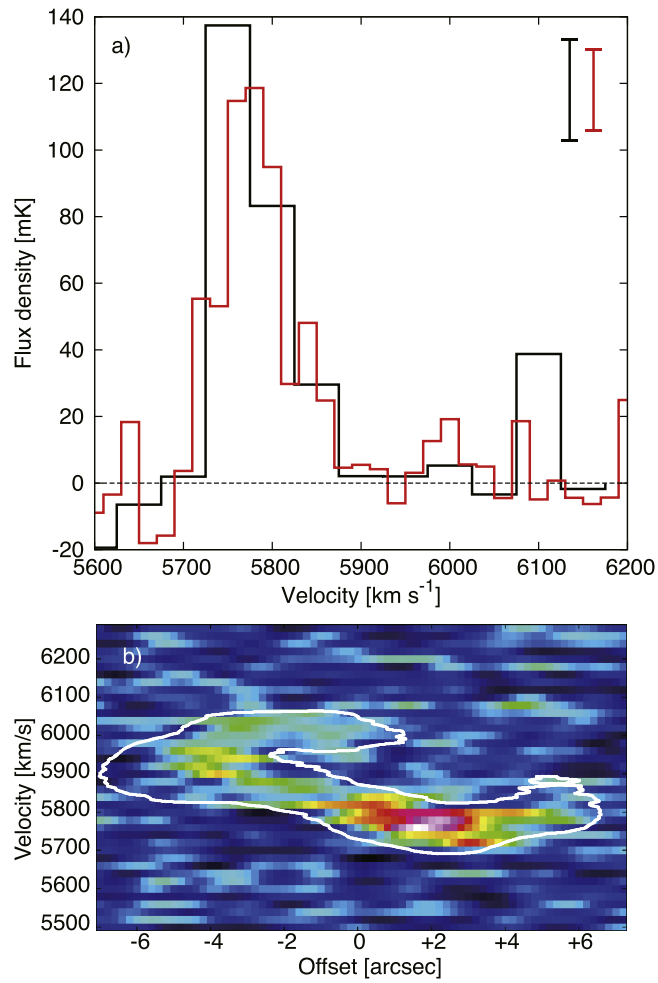

Figure 3. (a) Observed spectrum of CH_3OH (2_K–1_K) (black) and CH_3OH (3_K–2_K) (red) toward Region 6 (see Figure 2(a)). The bars shown in the top right represent typical statistical error bars associated with the data. (b) Position–velocity diagram of CH_3OH along the filament of VV 114 (position angle = 79°.4, length = 14″.2, and width = 1″.8). The white outline shows the 20σ contour of CO (1–0) (Saito et al. 2015).

where W_ν is the flux density, S_i is the line strength, μ_0 is the dipole moment, ν_i is the frequency of the transition, Q_{rot} is the rotational partition function, k is the Boltzmann constant, h is the Planck constant, T_{bg} is the cosmic microwave background temperature (=2.73 K), and E_u is the upper-state energy. We take the transition parameters necessary for calculating the equation (Table 1) from Splatalogue (see footnote 12) and the Cologne Database for Molecular Spectroscopy[13] (Müller et al. 2001, 2005).

We performed the calculation for 11 apertures of 3″ diameter along the filament shown in Figure 2, and an example for Region 6 is shown in Figure 4(a). Parameters used for the calculation and the results are listed in Table 2. Each point in Figure 4(a) corresponds to the upper-state column density of each unresolved transition, which decomposed by using the best-fit T_{rot}. The average T_{rot} is 7.4 ± 0.5 K for regions detected in both blended CH_3OH sets (i.e., Region 5–8). For regions without CH_3OH (2_K–1_K) detection (Region 1–4 and 9–11), we used T_{rot} = 7.4 K to derive N_{CH_3OH}. The average N_{CH_3OH} is (2.3 ± 1.0) × 10^{14} cm^{-2}, although this is an average

[13] http://www.astro.uni-koeln.de/cdms/catalog#partition

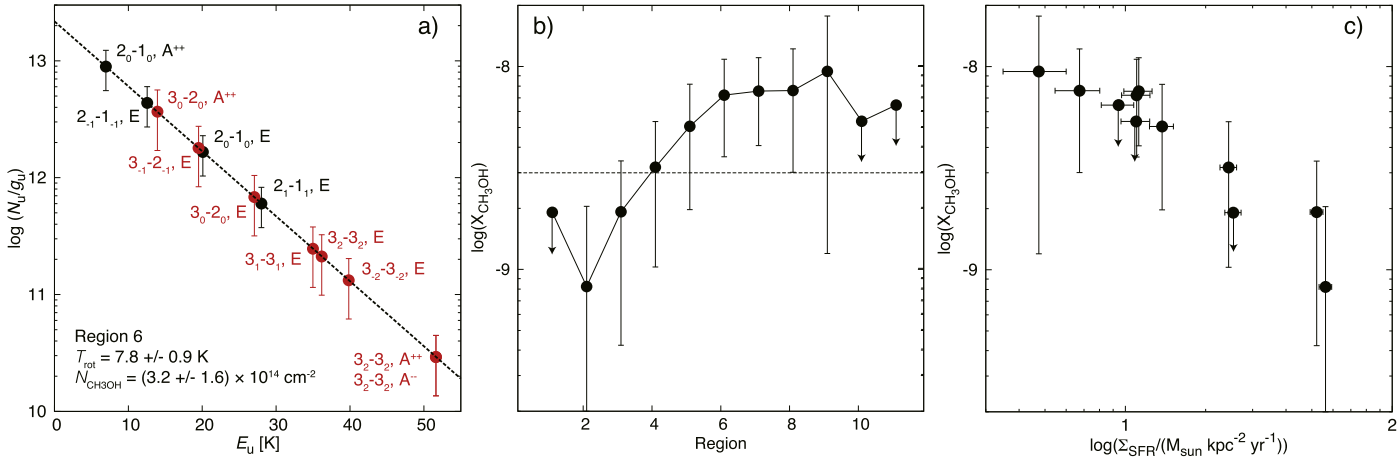

Figure 4. (a) Rotation diagram of CH_3OH for Region 6. Black and red points show $J = 2$–1 and 3–2 transitions, respectively. The dotted line shows the best fit. (b) X_{CH_3OH} distribution along the dust filament of VV 114. The arrows show the 3σ upper limits. The dashed line shows $X_{CH_3OH} \sim 3 \times 10^{-9}$, which is the value for the spiral arm of M51 using ~1 kpc aperture (Watanabe et al. 2014). (c) X_{CH_3OH} as a function of Σ_{SFR}.

of the beam-averaged column densities due to the uncorrected beam filling factor (η_{bf}). To ignore the unknown η_{bf} effect, we divided the N_{CH_3OH} by the H_2 column density ($N_{CH_3OH}/N_{H_2} = X_{CH_3OH}$), assuming that the N_{H_2} tracer has the same η_{bf}. In this paper, we employed the 880 μm dust continuum map (Figure 2(a)) to derive molecular gas mass (i.e., N_{H_2}) using the formulation described in Scoville et al. (2016). Assuming a constant dust temperature (T_{dust}) of 25 K, we derived X_{CH_3OH} along the filament. As shown in Figure 4(b), the X_{CH_3OH} distribution is clearly peaked around Overlap (Region 6–8), whereas the AGN (Region 1) and SB (Region 3) positions show almost an order of magnitude lower values. The errors shown in Figure 4(b) do not include the systematic uncertainty due to the 880 μm to N_{H_2} conversion.

The adopted T_{rot} of 7.4 K for Region 1–2 and 9–11 is consistent with the nondetections of the observed CH_3OH (2_K–1_K) flux, although Region 3 and 4 should be detected when assuming 7.4 K. This might be attributed to (a) higher T_{rot} than 7.4 K and/or (b) CH_3OH (3_K–2_K) overestimation due to a contamination from c-C_3H_2 (3_{12}–2_{21}) emission. In case (a), since we need to increase T_{rot} to ~10 K at least, the derived N_{CH_3OH} will decrease (~20%), and thus X_{CH_3OH} will decrease. In case (b), the intrinsic CH_3OH (3_K–2_K) fluxes will decrease 15% and 30% at Region 3 and 4, respectively, so that X_{CH_3OH} will decrease. For both cases, X_{CH_3OH} will decrease by a few tens of % around the eastern nucleus, so that our discussion and conclusion will not change. We note that the global X_{CH_3OH} trend is robust even if AGN and SB have higher T_{rot} and T_{dust} conditions, since X_{CH_3OH} only increases twice at most when adopting $T_{rot} = 7.4$–14.8 K and $T_{dust} = 25$–50 K.

Comparing with CH_3OH observations toward giant molecular complexes in the spiral arm of M51 with 1 kpc resolution ($X_{CH_3OH} \sim 3 \times 10^{-9}$; Watanabe et al. 2014) as a reference of the extragalactic (i.e., kpc scale) quiescent regions, Region 1–3 of VV 114 show a few times lower X_{CH_3OH}, although Region 5–9 show a few times higher X_{CH_3OH}.

5. DISCUSSION AND SUMMARY

To understand the characteristic CH_3OH distribution along the filament of VV 114, we compare X_{CH_3OH} with star formation rate surface density (Σ_{SFR}) as shown in Figure 4(c). We employed 110 GHz continuum (Saito et al. 2015), assuming that free–free (bremsstrahlung) emission dominates, and applied the free–free flux to SFR conversion (e.g., Yun & Carilli 2002). Such assumption is appropriate for starburst galaxies (e.g., M82; Condon 1992) and starburst-dominated LIRGs (e.g., NGC 1614; Saito et al. 2016). The 110 GHz image has a similar MRS (~21″) and synthesized beam (~2″) to CH_3OH images. We note that Σ_{SFR} for Region 1 and Region 2 are upper limits, because of the presence of the putative AGN (i.e., contribution from nonthermal synchrotron emission). The derived log Σ_{SFR} shows a decreasing trend as a function of X_{CH_3OH} with the correlation coefficient of −0.94. When we exclude a putative AGN contribution (i.e., Region 2), the correlation coefficient becomes −0.97. This can be explained by efficient photodissociation of CH_3OH due to massive star formation and putative AGN in the nuclear region (e.g., Martín et al. 2009) or desorption of CO (i.e., the precursor molecule of CH_3OH) from dust-grain surfaces into gas phase before forming CH_3OH molecules due to initial high-temperature conditions. This is consistent with two orders of magnitude lower Σ_{SFR} at the spiral arm of M51 (Watanabe et al. 2014).

However, the photodissociation scenario is not enough to fully explain the CH_3OH distribution in VV 114, because Overlap shows higher X_{CH_3OH} and also higher Σ_{SFR} than M51. Thus, we need another efficient mechanism, such as hot-core or shock, in order to explain high X_{CH_3OH} at Overlap. Here, we estimate a possible CH_3OH (2_K–1_K) flux assuming that hot-core-like environments dominate Overlap. We used a single-dish measurement toward one of the local hot-cores NGC 2264 CMM3 (deconvolved major FWHM ~ 0.076 pc, $M = 40\,M_\odot$, $I_{CH_3OH(2_K-1_K)} = 39.7$ K km s^{-1}, $D = 738$ pc), which is believed to form a massive star of 8 $M_\odot$ (Watanabe et al. 2015, and references therein). To account for all the molecular gas mass of Region 6 (~8.1 × $10^8\,M_\odot$) of VV 114, we need ~2.0 × 10^7 CMM3. Since the CH_3OH (2_K–1_K) flux of CMM3 at 87 Mpc is ~2.9 × 10^{-9} K km s^{-1}, the total flux of CMM3-like hot-cores at Region 6 is ~0.058 K km s^{-1}. This is 0.5% of the observed CH_3OH (2_K–1_K) flux at Region 6 (11.9 ± 1.4 K km s^{-1}). On average, between Region 5 and Region 9, the possible contribution from hot-core-like environments is only 0.6%. When we use other representative hot-core environments OMC-1, Sgr B2(N), and Sgr B2(M) (Lis et al. 1993; Jones et al. 2008; Bally et al. 2011; Watanabe et al.

Table 2
Information of the Rotation Diagram and Gas and Star Formation Properties

ID	R.A. (°)	Decl. (°)	$S_{2_K-1_K}\,dv$ (Jy km s^{-1})	$S_{3_K-2_K}\,dv$ (Jy km s^{-1})	$T_{\rm rot}$[a] (K)	$N_{\rm CH_3OH}$ (10^{14} cm^{-2})	$\Sigma_{\rm SFR}$[b] ($M_\odot$ kpc^{-2} yr^{-1})	$N_{\rm H_2}$[c] (10^{22} cm^{-2})	$X_{\rm CH_3OH}$ (10^{-9})
1	16.9485	−17.5067	<0.26	<0.32	…	<0.9	25.4 ± 1.8	4.7 ± 0.4	<1.9
2	16.9482	−17.5070	<0.27	0.29 ± 0.08	…	0.8 ± 1.2	56.3 ± 3.1	9.8 ± 1.0	0.8 ± 1.2
3	16.9478	−17.5072	<0.26	0.68 ± 0.10	…	1.9 ± 1.5	52.1 ± 2.9	9.8 ± 1.0	1.9 ± 1.5
4	16.9474	−17.5072	<0.27	0.85 ± 0.11	…	2.4 ± 1.6	24.4 ± 1.7	7.4 ± 0.6	3.2 ± 2.2
5	16.9470	−17.5072	0.44 ± 0.09	0.81 ± 0.11	6.1 ± 0.7	2.9 ± 1.7	13.7 ± 1.4	5.6 ± 0.5	5.1 ± 3.1
6	16.9465	−17.5073	0.51 ± 0.09	1.20 ± 0.12	7.8 ± 0.9	3.2 ± 1.6	11.0 ± 1.3	4.5 ± 0.5	7.2 ± 3.6
7	16.9461	−17.5074	0.57 ± 0.09	1.20 ± 0.11	7.0 ± 0.7	3.6 ± 1.6	11.2 ± 1.4	4.7 ± 0.4	7.6 ± 3.5
8	16.9457	−17.5075	0.33 ± 0.07	0.86 ± 0.11	8.9 ± 1.5	2.1 ± 1.2	6.7 ± 1.3	2.8 ± 0.3	7.6 ± 4.6
9	16.9453	−17.5076	<0.26	0.56 ± 0.09	…	1.6 ± 1.3	4.7 ± 1.3	1.6 ± 0.3	9.5 ± 8.3
10	16.9449	−17.5076	<0.26	<0.32	…	<0.9	11.0 ± 1.4	1.7 ± 0.3	<5.4
11	16.9444	−17.5077	<0.26	<0.32	…	<0.9	9.4 ± 1.3	1.4 ± 0.3	<6.5

Notes.
[a] For regions without CH_3OH (2_K–1_K) detection, we adopt 7.4 K to derive $N_{\rm CH_3OH}$.
[b] Star formation rate surface density derived from the 110 GHz continuum emission (Saito et al. 2015).
[c] Molecular hydrogen column density derived from the 880 μm dust continuum emission (Saito et al. 2015).

Table 3
Contribution of some Representative Hot-cores to Region 6

	Unit	NGC 2264 CMM3	OMC-1	Sgr B2(N)	Sgr B2(M)
Distance	pc	738	437	8.34×10^3	8.34×10^3
Mass	$M_\odot$	40	60–80	9100	2900
$I_{\rm CH_3OH(2_K-1_K)}$	K km s^{-1}	39.7	309	907	1114
# of hot-core at Region 6		2.0×10^7	$(1.0–1.4) \times 10^7$	8.9×10^4	2.8×10^5
$I_{\rm CH_3OH(2_K-1_K)}$ at 87 Mpc	K km s^{-1}	2.9×10^{-9}	7.8×10^{-9}	8.3×10^{-6}	1.0×10^{-5}
$I_{\rm CH_3OH(2_K-1_K)}$ from hot-cores at Region 6	%	0.5	0.7–0.9	6.2	23.5

2015) instead of NGC 2264 CMM3, the contribution from hot-cores at Region 6 is still small (0.7%–0.9%, 6.2%, and 23.5%, respectively). We list parameters used for these comparisons in Table 3. We note that the derived percentages are upper limits, because we assumed an extreme case that all gas masses contained in Region 6 are associated to hot-cores. Similar estimation of a possible CH_3OH flux from large collections of a molecular outflow from a massive star shows a similar conclusion (Meier et al. 2014). Therefore, we suggest that kpc-scale shocks are only applicable mechanisms to explain the high $X_{\rm CH_3OH}$ at Overlap. The possible origin of the large-scale shocks is a gas-rich galaxy–galaxy collision, because Overlap is located between the progenitor's galaxies without apparent progenitor's spiral arms, bars, or nuclei. This shocked CH_3OH scenario at Overlap is consistent with the explanation of large velocity dispersion components of ionized gas detected at the same region (Rich et al. 2011). The shocked ionized gas shows the same systemic velocity as the CH_3OH. This shows the evidence that ionized gas shocks colocate with molecular gas shocks at Overlap, indicating that merger-induced shocks can affect both molecular and ionized gas ISM.

In summary, merger-induced shocks are the most likely scenario to explain the kpc-scale CH_3OH filament (and large dispersion components of ionized gas) across the progenitors of VV 114. The $X_{\rm CH_3OH}$ distribution peaks at Overlap, although the eastern nucleus, which harbors dense clumps associated with a compact starburst and a putative AGN, shows almost an order of magnitude lower abundances. $X_{\rm CH_3OH}$ clearly anticorrelates with $\Sigma_{\rm SFR}$, indicating that strong photodissociation (i.e., efficient destruction) or desorption of CO (i.e., inefficient production) on dust grains due to star-forming activities or AGN plays an important role to suppress CH_3OH emission at the nuclear regions. This is the first result of merger-induced shocks in molecular gas ISM through CH_3OH lines. As a future development, higher-J CH_3OH observations are required to address more realistic, finite optical depth and non-LTE excitation conditions (e.g., Goldsmith & Langer 1999; Mangum & Shirley 2015). Avoiding the multiple K-ladder blending, isolated transitions (e.g., $J_K = 0_0$–1_{-1} at 108.89396 GHz) are also important. Followup observations of shock tracers in other wavelengths (e.g., near-IR warm H_2; Sugai et al. 1999; Herrera et al. 2012) can be used to confirm the shock scenario at Overlap. We will discuss other molecular lines detected and not detected in the Band 3 and Band 4 spectral scan in a forthcoming paper.

The authors thank an anonymous referee for constructive comments that improved the contents of this paper. The authors thank S. Aalto, R. Aladro, P. Sanhueza, Y. Shimajiri, and K. Sliwa for useful discussion. TS and the other authors thank the ALMA staff for their kind support, and H. Nagai for the instruction of ALMA data reduction. TS and ML are financially supported by a Research Fellowship from the Japan Society for the Promotion of Science for Young Scientists. TS was supported by the ALMA Japan Research Grant of NAOJ Chile Observatory, NAOJ-ALMA-0089, NAOJ-ALMA-0105, and NAOJ-ALMA-0114. RK was supported by JSPS KAKENHI grant number 15H02073. DI was supported by JSPS KAKENHI grant number 15H02074. This paper makes use of the following ALMA data: ADS/JAO.ALMA#2011.0.00467.S and ADS/JAO.ALMA#2013.1.01057.S. ALMA is a partnership of ESO (representing its member states), NSF (USA) and NINS (Japan),

together with NRC (Canada), NSC and ASIAA (Taiwan), and KASI (Republic of Korea), in cooperation with the Republic of Chile. The joint ALMA Observatory is operated by ESO, AUI/NRAO, and NAOJ.

REFERENCES

Aladro, R., Martín, S., Martín-Pintado, J., et al. 2011, A&A, 535, A84
Aladro, R., Martín, S., Riquelme, D., et al. 2015, A&A, 579, A101
Armus, L., Mazzarella, J. M., Evans, A. S., et al. 2009, PASP, 121, 559
Bally, J., Cunningham, N. J., Moeckel, N., et al. 2011, ApJ, 727, 113
Condon, J. J. 1992, ARA&A, 30, 575
Costagliola, F., Aalto, S., Rodriguez, M. I., et al. 2011, A&A, 528, A30
Costagliola, F., Sakamoto, K., Muller, S., et al. 2015, A&A, 582, A91
Davis, T. A., Heiderman, A., Evans, N. J., & Iono, D. 2013, MNRAS, 436, 570
Frayer, D. T., Ivison, R. J., Smail, I., Yun, M. S., & Armus, L. 1999, AJ, 118, 139
Galametz, M., Zhang, Z.-Y., Immer, K., et al. 2016, arXiv:1606.06225
García-Burillo, S., Usero, A., Fuente, A., et al. 2010, A&A, 519, A2
Garrod, R. T., Widicus Weaver, S. L., & Herbst, E. 2008, ApJ, 682, 283
Goldader, J. D., Meurer, G., Heckman, T. M., et al. 2002, ApJ, 568, 651
Goldsmith, P. F., & Langer, W. D. 1999, ApJ, 517, 209
Grimes, J. P., Heckman, T., Hoopes, C., et al. 2006, ApJ, 648, 310
Henkel, C., Jacq, T., Mauersberger, R., Menten, K. M., & Steppe, H. 1987, A&A, 188, L1
Herrera, C. N., Boulanger, F., Nesvadba, N. P. H., & Falgarone, E. 2012, A&A, 538, L9
Iono, D., Ho, P. T. P., Yun, M. S., et al. 2004, ApJL, 616, L63
Iono, D., Saito, T., Yun, M. S., et al. 2013, PASJ, 65, 7
Jones, P. A., Burton, M. G., Cunningham, M. R., et al. 2008, MNRAS, 386, 117
Lee, H.-H., Bettens, R. P. A., & Herbst, E. 1996, A&AS, 119, 111
Lis, D. C., Goldsmith, P. F., Carlstrom, J. E., & Scoville, N. Z. 1993, ApJ, 402, 238
Mangum, J. G., & Shirley, Y. L. 2015, PASP, 127, 266
Martín, S., Krips, M., Martín-Pintado, J., et al. 2011, A&A, 527, A36
Martín, S., Martín-Pintado, J., & Mauersberger, R. 2006a, A&A, 450, L13
Martín, S., Martín-Pintado, J., & Viti, S. 2009, ApJ, 706, 1323
Martín, S., Mauersberger, R., Martín-Pintado, J., Henkel, C., & García-Burillo, S. 2006b, ApJS, 164, 450
Mathys, G. 2013, ALMA Cycle 2 Proposers Guide, Version 1.8, ALMA
McMullin, J. P., Waters, B., Schiebel, D., Young, W., & Golap, K. 2007, adass XVI, 376, 127
Meier, D. S., & Turner, J. L. 2005, ApJ, 618, 259
Meier, D. S., & Turner, J. L. 2012, ApJ, 755, 104
Meier, D. S., Turner, J. L., & Beck, S. C. 2014, ApJ, 795, 107
Müller, H. S. P., Schlöder, F., Stutzki, J., & Winnewisser, G. 2005, JMoSt, 742, 215
Müller, H. S. P., Thorwirth, S., Roth, D. A., & Winnewisser, G. 2001, A&A, 370, L49
Nakajima, T., Takano, S., Kohno, K., et al. 2015, PASJ, 67, 8
Nishimura, Y., Shimonishi, T., Watanabe, Y., et al. 2016, arXiv:1608.01099
Rabli, D., & Flower, D. R. 2010, MNRAS, 406, 95
Rich, J. A., Kewley, L. J., & Dopita, M. A. 2011, ApJ, 734, 87
Saito, T., Iono, D., Xu, C. K., et al. 2016, PASJ, 68, 20
Saito, T., Iono, D., Yun, M. S., et al. 2015, ApJ, 803, 60
Saitoh, T. R., Daisaka, H., Kokubo, E., et al. 2009, PASJ, 61, 481
Schutte, W. A., Tielens, A. G. G., & Sandford, S. A. 1991, ApJ, 382, 523
Scoville, N., Sheth, K., Aussel, H., et al. 2016, ApJ, 824, 63
Scoville, N. Z., Evans, A. S., Thompson, R., et al. 2000, AJ, 119, 991
Sliwa, K., Wilson, C. D., Krips, M., et al. 2013, ApJ, 777, 126
Sugai, H., Davies, R. I., Malkan, M. A., et al. 1999, ApJ, 527, 778
Takano, S., Nakajima, T., Kohno, K., et al. 2014, PASJ, 66, 75
Tateuchi, K., Konishi, M., Motohara, K., et al. 2015, ApJS, 217, 1
Teyssier, R., Chapon, D., & Bournaud, F. 2010, ApJL, 720, L149
Usero, A., García-Burillo, S., Martín-Pintado, J., Fuente, A., & Neri, R. 2006, A&A, 448, 457
Viti, S., Jimenez-Serra, I., Yates, J. A., et al. 2011, ApJL, 740, L3
Watanabe, N., Shiraki, T., & Kouchi, A. 2003, ApJL, 588, L121
Watanabe, Y., Sakai, N., López-Sepulcre, A., et al. 2015, ApJ, 809, 162
Watanabe, Y., Sakai, N., Sorai, K., & Yamamoto, S. 2014, ApJ, 788, 4
Wilson, C. D., Petitpas, G. R., Iono, D., et al. 2008, ApJS, 178, 189
Yun, M. S., & Carilli, C. L. 2002, ApJ, 568, 88
Yun, M. S., Scoville, N. Z., & Knop, R. A. 1994, ApJL, 430, L109